

Dual modality optical coherence and whole-body photoacoustic tomography imaging of chick embryos in multiple development stages

Mengyang Liu,¹ Barbara Maurer,² Boris Hermann,¹ Behrooz Zabihian,¹ Michelle G. Sandrian,³ Angelika Unterhuber,¹ Bernhard Baumann,¹ Edward Z. Zhang,⁴ Paul C. Beard,⁴ Wolfgang J. Weninger,² and Wolfgang Drexler^{1,*}

¹Center for Medical Physics and Biomedical Engineering, Medical University of Vienna, AKH 4L, Währinger Gürtel 18-20, Vienna 1090, Austria

²Center for Anatomy and Cell Biology, Medical University of Vienna, Währinger Straße 13, Vienna 1090, Austria

³Department of Ophthalmology, University of Pittsburgh, Eye & Ear Institute, 203 Lothrop Street, Pittsburgh, PA 15213, USA

⁴Department of Medical Physics and Bioengineering, University College London, Shropshire House, 11-20 Capper Street, London WC1E 6JA, UK

*wolfgang.drexler@meduniwien.ac.at

Abstract: Chick embryos are an important animal model for biomedical studies. The visualization of chick embryos, however, is limited mostly to postmortem sectional imaging methods. In this work, we present a dual modality optical imaging system that combines swept-source optical coherence tomography and whole-body photoacoustic tomography, and apply it to image chick embryos at three different development stages. The explanted chick embryos were imaged *in toto* with complementary contrast from both optical scattering and optical absorption. The results serve as a prelude to the use of the dual modality system in longitudinal whole-body monitoring of chick embryos *in ovo*.

©2014 Optical Society of America

OCIS codes: (170.4500) Optical coherence tomography; (170.5120) Photoacoustic imaging; (170.3880) Medical and biological imaging.

References and links

1. K. H. Kain, J. W. I. Miller, C. R. Jones-Paris, R. T. Thomason, J. D. Lewis, D. M. Bader, J. V. Barnett, and A. Zijlstra, "The chick embryo as an expanding experimental model for cancer and cardiovascular research," *Dev. Dyn.* **243**(2), 216–228 (2014).
2. H. S. Leong, N. F. Steinmetz, A. Ablack, G. Destito, A. Zijlstra, H. Stuhlmann, M. Manchester, and J. D. Lewis, "Intravital imaging of embryonic and tumor neovasculature using viral nanoparticles," *Nat. Protoc.* **5**(8), 1406–1417 (2010).
3. L. Yang, S. You, L. Zhang, T. Yang, P. Li, and J. Lu, "Noninvasive vasculature detection using laser speckle imaging in avian embryos through intact egg in early incubation stage," *Biomed. Opt. Express* **4**(1), 32–37 (2013).
4. P. K. Rastogi, L. Pflug, and R. Delez, "Noninvasive observation of embryonic behavior in chicks using holographic interference," *Appl. Opt.* **28**(7), 1378–1381 (1989).
5. S. N. B. Bone, G. A. P. Johnson, and M. B. D. V. M. P. Thompson, "Three-Dimensional Magnetic Resonance Microscopy of the Developing Chick Embryo," *Invest. Radiol.* **21**(10), 782–787 (1986).
6. X. Li, J. Liu, M. Davey, S. Duce, N. Jaber, G. Liu, G. Davidson, S. Tenent, R. Mahood, P. Brown, C. Cunningham, A. Bain, K. Beattie, L. McDonald, K. Schmidt, M. Towers, C. Tickle, and S. Chudek, "Magnetic resonance imaging of avian embryos," *J. Anat.* **211**(6), 798–809 (2007).
7. A. J. Ewald, H. McBride, M. Reddington, S. E. Fraser, and R. Kerschmann, "Surface imaging microscopy, an automated method for visualizing whole embryo samples in three dimensions at high resolution," *Dev. Dyn.* **225**(3), 369–375 (2002).
8. W. J. Weninger, S. H. Geyer, T. J. Mohun, D. Rasskin-Gutman, T. Matsui, I. Ribeiro, L. F. Costa, J. C. Ispisua-Belmonte, and G. B. Müller, "High-resolution episcopic microscopy: a rapid technique for high detailed 3D analysis of gene activity in the context of tissue architecture and morphology," *Anat. Embryol. (Berl.)* **211**(3), 213–221 (2006).
9. J. Sharpe, U. Ahlgren, P. Perry, B. Hill, A. Ross, J. Hecksher-Sørensen, R. Baldock, and D. Davidson, "Optical projection tomography as a tool for 3D microscopy and gene expression studies," *Science* **296**(5567), 541–545 (2002).

10. T. Ichikawa, K. Nakazato, P. J. Keller, H. Kajiuura-Kobayashi, E. H. K. Stelzer, A. Mochizuki, and S. Nonaka, "Live imaging and quantitative analysis of gastrulation in mouse embryos using light-sheet microscopy and 3D tracking tools," *Nat. Protoc.* **9**(3), 575–585 (2014).
11. P. J. Keller and H.-U. Dodt, "Light sheet microscopy of living or cleared specimens," *Curr. Opin. Neurobiol.* **22**(1), 138–143 (2012).
12. M. Masyuk, G. Morosan-Puopolo, B. Brand-Saberi, and C. Theiss, "Combination of *in ovo* electroporation and time-lapse imaging to study migrational events in chicken embryos," *Dev. Dyn.* **243**(5), 690–698 (2014).
13. C. E. Miller, R. P. Thompson, M. R. Bigelow, G. Gittinger, T. C. Trusk, and D. Sedmera, "Confocal imaging of the embryonic heart: how deep?" *Microsc. Microanal.* **11**(3), 216–223 (2005).
14. M. W. Jenkins, O. Q. Chughtai, A. N. Basavanahally, M. Watanabe, and A. M. Rollins, "In vivo gated 4D imaging of the embryonic heart using optical coherence tomography," *J. Biomed. Opt.* **12**(3), 030505 (2007).
15. S.-L. Chen, J. Burnett, D. Sun, X. Wei, Z. Xie, and X. Wang, "Photoacoustic microscopy: a potential new tool for evaluation of angiogenesis inhibitor," *Biomed. Opt. Express* **4**(11), 2657–2666 (2013).
16. W. Drexler and F. G. James, *Optical Coherence Tomography, Technology and Applications* (Springer, 2008).
17. L. V. Wang, "Tutorial on Photoacoustic Microscopy and Computed Tomography," *IEEE J. Sel. Top. Quantum Electron.* **14**(1), 171–179 (2008).
18. W. Drexler, M. Liu, A. Kumar, T. Kamali, A. Unterhuber, and R. A. Leitgeb, "Optical coherence tomography today: speed, contrast, and multimodality," *J. Biomed. Opt.* **19**(7), 071412 (2014).
19. J. Xia and L. V. Wang, "Small-animal whole-body photoacoustic tomography: a review," *IEEE Trans. Biomed. Eng.* **61**(5), 1380–1389 (2014).
20. J. Laufer, F. Norris, J. Cleary, E. Zhang, B. Treeby, B. Cox, P. Johnson, P. Scambler, M. Lythgoe, and P. Beard, "In vivo photoacoustic imaging of mouse embryos," *J. Biomed. Opt.* **17**(6), 061220 (2012).
21. E. Z. Zhang, B. Povazay, J. Laufer, A. Alex, B. Hofer, B. Pedley, C. Glittenberg, B. Treeby, B. Cox, P. Beard, and W. Drexler, "Multimodal photoacoustic and optical coherence tomography scanner using an all optical detection scheme for 3D morphological skin imaging," *Biomed. Opt. Express* **2**(8), 2202–2215 (2011).
22. W. Drexler, M. Liu, A. Kumar, T. Kamali, A. Unterhuber, and R. A. Leitgeb, "Optical coherence tomography today: speed, contrast, and multimodality," *J. Biomed. Opt.* **19**(7), 071412 (2014).
23. M. Liu, N. Schmitner, M. G. Sandrian, B. Zabihian, B. Hermann, W. Salvenmoser, D. Meyer, and W. Drexler, "In vivo spectroscopic photoacoustic tomography imaging of a far red fluorescent protein expressed in the exocrine pancreas of adult zebrafish," *Proc. SPIE* **8943**, 142 (2014).
24. M. Liu, N. Schmitner, M. G. Sandrian, B. Zabihian, B. Hermann, W. Salvenmoser, D. Meyer, and W. Drexler, "In vivo three dimensional dual wavelength photoacoustic tomography imaging of the far red fluorescent protein E2-Crimson expressed in adult zebrafish," *Biomed. Opt. Express* **4**(10), 1846–1855 (2013).
25. V. Hamburger and H. L. Hamilton, "A series of normal stages in the development of the chick embryo. 1951," *Dev. Dyn.* **195**(4), 231–272 (1992).
26. E. Zhang, J. Laufer, and P. Beard, "Backward-mode multiwavelength photoacoustic scanner using a planar Fabry-Perot polymer film ultrasound sensor for high-resolution three-dimensional imaging of biological tissues," *Appl. Opt.* **47**(4), 561–577 (2008).
27. B. E. Treeby and B. T. Cox, "k-Wave: MATLAB toolbox for the simulation and reconstruction of photoacoustic wave fields," *J. Biomed. Opt.* **15**(2), 021314 (2010).
28. "American National Standard for Safe Use of Lasers," American National Standards Institute **ANSI Z136.1** (2007).
29. B. Maurer, S. H. Geyer, and W. J. Weninger, "A chick embryo with a yet unclassified type of cephalothoracopagus malformation and a hypothesis for explaining its genesis," *Anat. Histol. Embryol.* **42**(3), 191–200 (2013).
30. J. Schindelin, I. Arganda-Carreras, E. Frise, V. Kaynig, M. Longair, T. Pietzsch, S. Preibisch, C. Rueden, S. Saalfeld, B. Schmid, J.-Y. Tinevez, D. J. White, V. Hartenstein, K. Eliceiri, P. Tomancak, and A. Cardona, "Fiji: an open-source platform for biological-image analysis," *Nat. Methods* **9**(7), 676–682 (2012).
31. T. Hiruma and R. Hirakow, "Formation of the pharyngeal arch arteries in the chick embryo. Observations of corrosion casts by scanning electron microscopy," *Anat. Embryol. (Berl.)* **191**(5), 415–423 (1995).
32. B. J. Martinsen, "Reference guide to the stages of chick heart embryology," *Dev. Dyn.* **233**(4), 1217–1237 (2005).
33. D. A. T. New, "A new technique for the cultivation of the chick embryo *in vitro*," *J. Embryol. Exp. Morphol.* **3**, 326–331 (1955).

1. Introduction

The chick embryo has been studied since the time of Aristotle [1]. Over the centuries, it has gradually been established as an important model organism, extensively used in developmental and cancer biology. This is due to its biological similarity to humans [1], the accessibility of the embryo for *in vivo* surgery and experiments, and because direct *in ovo* studies of developing embryos can be accomplished with the aid of relatively simple optical settings. The natural immunodeficiency of chick embryos makes them especially amenable for tumor xenografting in their vascular chorioallantoic membrane (CAM), which serves as a valuable model for tumor angiogenesis, and this procedure is relatively easy and well established [1, 2]. In developmental biology, the chick embryo also offers a platform for

investigating the effects physical alterations of embryonic structures have on morphogenesis and on developmental success of the embryo, which provides a unique opportunity for studying the mechanisms underlying cardiovascular remodeling and the genesis of cardiovascular malformations. While the protocol for imaging the CAM on the surface of the culture is relatively straightforward, visualizing the organ systems – especially the vasculature of older embryos – without destroying the integrity of the embryo remains a challenge.

Efforts have been made to use laser speckle imaging (LSI) for noninvasive detection of the vasculature of chick embryos in early stages of incubation [3], but the achievable resolution makes LSI more a method for the selection and exclusion of unfertilized eggs than a way to visualize the blood vessels in embryos. Holographic interference was also used to monitor the intact egg shell as an indication of embryo behavior [4], but this method was not able to visualize embryonic organs or tissues. Magnetic resonance (MR) microscopy [5] and micro-magnetic resonance imaging (μ MRI) [6] provided images of major structures and organs of avian embryos. The hours-long data acquisition time, the relatively low resolution and the lack of contrast for hemoglobin, however, make it suboptimal. Other imaging methods, such as conventional and advanced histology, surface imaging microscopy (SIM) [7], high resolution episcopic microscopy (HREM) [8], optical projection tomography (OPT) [9] and light sheet microscopy [10, 11], can show minute structures and volume displays of chick embryos, but are inherently destructive. They either require mechanical sectioning of sacrificed and fixed embryos and the use of exogenous contrast agents to distinguish the embryonic tissues and organs, or require harvested embryos and lengthy imaging sessions. Multiphoton microscopy and time-lapse confocal microscopy [12, 13] have also been used for chick embryo imaging. Although cellular level information may be retrieved and *in vivo* studies can be performed for cultured tissues, both methods are highly limited in imaging depth, preventing them for whole-body use.

Optical coherence tomography (OCT) which has high resolution and rapid acquisition speed, was successfully applied to image the chick heart *in vivo* by gating the imaging cycles using laser Doppler velocimetry (LDV) [14]. The results demonstrated the potential of OCT for monitoring cardiac defects in chick embryos using morphological information based on optical scattering properties of tissues. Photoacoustic microscopy (PAM), with hemoglobin as an endogenous contrast mechanism, was used to measure the microvasculature density on the CAM as a tool for angiogenesis inhibitor evaluation [15]. Since OCT image contrast originates from the differences in the optical scattering [16], and photoacoustic image contrast is derived from the absorption of chromophores such as hemoglobin [17], dual modality OCT/photoacoustic imaging systems can provide co-registered, complementary information from biological samples with vasculature visualized by photoacoustic imaging and morphology provided by OCT [18]. For whole-body imaging on the order of cubic centimeters, photoacoustic tomography (PAT) provides deeper penetration depth than PAM. A planar-view PAT system based on a Fabry-Perot interferometric polymer film detector is of particular interest because of its simplicity of sample positioning and unique optical detection mechanisms [19]. Previous studies have demonstrated optical detection PAT for *in utero* mouse embryo imaging, where a penetration depth of beyond 6 mm was achieved with high resolution [20]. The combination of such a PAT system with a spectral domain OCT (SD-OCT) system was designed for morphological skin imaging and was used to image murine and human skin [21]. With the development of swept-source technologies, swept-source OCT (SS-OCT) offers the possibilities of higher acquisition speed, less sensitivity roll-off as well as the potential for extended imaging depth and speckle resolution [22]. Considering these features, a design combining an SS-OCT system with an optical detection PAT system was presented [23] while the performance and application of it were yet not adequately explored.

In this paper, we present a dual modality optical coherence and whole-body photoacoustic tomography system featuring a 1060 nm SS-OCT sub-system and an optical detection PAT sub-system for its application in chick embryo imaging. With improved resolution compared to the standalone system presented in [24] and the possibility to co-register the OCT and PAT images, embryos at three normal developmental stages were imaged by the dual modality

system. The three development stages imaged span from stage 21 to stage 29 according to the Hamburger & Hamilton (HH) criterion [25], representing a broadband morphological and cardiac development from embryo day 3.5 till day 6. After the dual modality imaging, the samples were prepared for HREM, which served as a structural reference for OCT/PAT whole-body chick embryo imaging.

2. Materials and methods

2.1 Dual modality OCT/PAT system

The schematic of the system is given in Fig. 1. The whole system consists of three major parts: the shared unit for 2D sample arm scanning in OCT and interrogation laser beam scanning in PAT, the SS-OCT unit employing a 1060 nm swept source (SSOCT-1060, Axsun Technologies, U.S.) and the optical detection PAT unit. The OCT swept source had a bandwidth of 120 nm and a sweep repetition rate of 100 kHz. The OCT sample arm power incident upon the embryos was measured to be 3.4 mW. The lateral and axial resolutions were experimentally determined by imaging a resolution target and a specular surface to be 20 μm and 5 μm , respectively in air. By using a neutral density filter mimicking soft tissue in the sample arm, a sensitivity of 94 dB was achieved by calculating the signal to noise ratio of the reconstructed image. The first dual balanced detector (DBD) and the free space Michelson interferometer were used for wavelength resampling. The working principle of optical detection PAT system can be found in [26]. To be succinct, the output of a 50 Hz optical parametric oscillator (OPO) (VersaScan/BB/HE, GWU-Lasertechnik Vertriebsges.mbH, Germany) pumped at 355 nm (Quanta-Ray Pro270-50, Spectra-Physics, U.S.) was coupled into two multimode fibers, one for signal output and the other for idler output. A CW laser operating in the telecom range was used to interrogate the Fabry-Perot interferometric polymer film sensor enabled by 2D scanning of a pair of galvanometer scanning mirrors (6210H, Cambridge Technology, U.S.). The passband of the polymer film sensor permits backward transmission of excitation above 600 nm, while the interrogation beam is reflected and fed into a customized transimpedance amplifier. When a photoacoustic pulse propagates to the polymer film sensor, the deformation caused by the acoustic pressure can be assumed to linearly modulate the reflected intensity of the interrogation beam. By synchronously scanning the interrogation beam over the polymer film sensor, 3D photoacoustic images can be formed using the time reversal algorithm provided in the k-wave toolbox [27] in which every detected pulse on the sensor is back-propagated in time to form the pressure source from which it originates. The lateral and axial resolutions of the PAT system were experimentally measured to be 79 μm and 42 μm , respectively. To measure the resolutions, a 1951 USAF resolution target (Edmund Optics Inc., U.S.) was placed 4.9 mm above the sensor with distilled water as the acoustic couplant. Backward illumination onto the chrome coating of the resolution target induced photoacoustic signals. After reconstruction with no upsampling of the raw data, the resolutions were acquired by calculating the line spread functions.

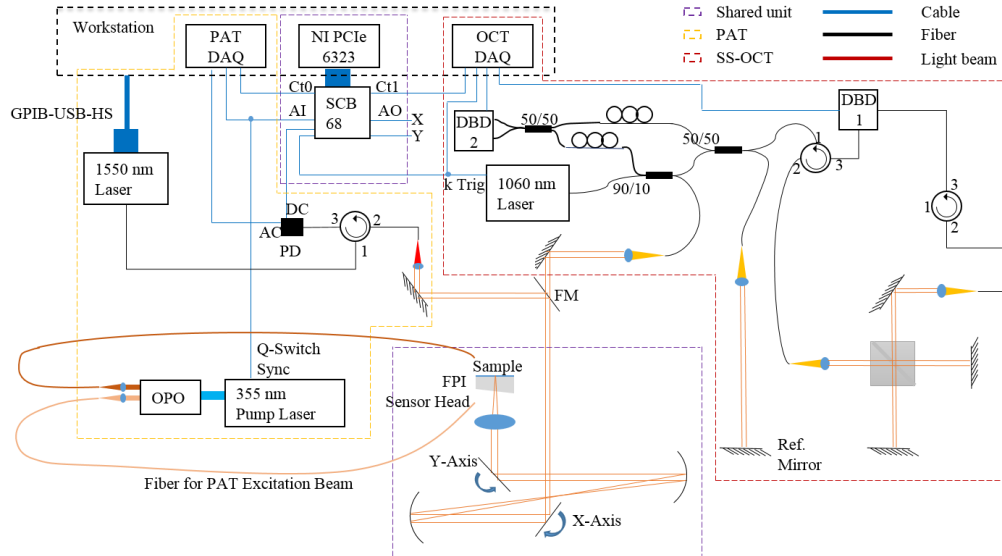


Fig. 1. Schematic of the dual modality OCT/PAT system. DAQ: data acquisition device; Ct: counter; PD: photodiode; AC & DC: the two output channels of the transimpedance amplifier using the PD; Ref.: reference; AI: analog input; AO: analog output; FPI: Fabry-Perot interferometer; FM: flip mirror; DBD: dual balanced detector. Adapted from [23].

2.2 Chick embryo preparation and imaging scheme

Fertilized eggs of white leghorn chick embryos were purchased from a hatchery (Schropper GmbH, Austria) and incubated on different days so that the imaging of stage HH21, HH 27 and HH29 embryos could be performed in the same session. The eggs were incubated at 38°C and 70% humidity until the time of imaging. Immediately prior to imaging, the embryos were explanted using microsurgical instruments and transferred to the top of the polymer film sensor with 4% paraformaldehyde as the acoustic couplant. Forward and backward illumination using the idler and signal output from the OPO, respectively, were used simultaneously to maximize the imaging depth. The two excitation wavelengths used were 845 nm and 609 nm with pulse energies of 11.7 mJ and 14 mJ, respectively, measured at the outputs of the corresponding fibers. The excitation fiber tips were placed several centimeters away from the sensor to guarantee an effective illumination area of a couple of square centimeters and hence an optical fluence below the safety limit of 20 mJ/cm² [28]. A photo of the scanner is provided in Fig. 2. The scan step size was set at 40 μm to cover an area of 1 cm × 1 cm for the stage HH21 and stage HH27 embryos in PAT imaging, followed by scan step sizes of 14.3 μm and 17.2 μm in their corresponding OCT scans. Given the large size of the stage HH29 embryos, a step size of 60 μm was used for PAT over an area of 1.3 cm × 1.4 cm while the step size of OCT for these embryos was 18.6 μm and 22.9 μm in the two orthogonal dimensions, respectively. The total data acquisition time for each complete data set was approximately 30 minutes including the switching time between the OCT and the PAT modes.

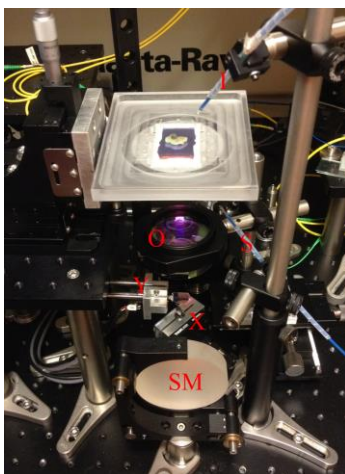


Fig. 2. Photo illustration of the OCT/PAT scanning unit. I: idler output from the OPO; S: signal output from the OPO; SM: spherical mirror; X: x-axis galvanometer scanning mirror; Y: y-axis galvanometer scanning mirror; O: objective scan lens.

Immediately after the OCT/PAT scan, the embryos were fixed in 4% paraformaldehyde buffered with phosphate-buffered saline (PBS) before being transferred into 70% ethanol for storage. One embryo from each of the three stages was selected to be imaged using HREM. HREM involves embedding the specimen in an eosin dyed resin block, which is mounted on a rotary microtome and sectioned in steps of a few μm with each section imaged by a fluorescence microscope prior to being sliced off; a detailed procedure is provided in [29]. The OCT/PAT data for the three HREM imaged embryos were then reconstructed and post-processed in MATLAB (MATLAB R2013a, The MathWorks, U.S.). 3D rendering, image registration and image fusion were performed using Fiji [30]. To fuse the volume data of both OCT and PAT for the same embryo, interpolation and re-slicing in the depth dimension for the data sets were applied, so that the re-sliced data sets of both OCT and PAT had the same depth increment. Similar procedure was done in the transverse dimensions to fully achieve the voxel match of the co-registered OCT and the PAT volumes. The 3D matched volumes for OCT and PAT were then assigned to different color channels – e.g. OCT in gray color channel while PAT in red color channel; finally these two color channels were merged to form the fused 3D volumes. In display, the intensity and opacity can be adjusted for each individual color channel, achieving the desired visual effect. The 3D segmentation was achieved in Amira (Amira 5.3.3, FEI Corporate, U.S.) by manually selecting the parts of interests.

3. Results

Figures 3(a)-3(c) are OCT maximum intensity projection (MIP) images of stage HH21, HH27 and HH29 embryos, respectively. Their corresponding PAT MIP images are given below in Fig. 3(d)-3(f). The general morphological differences between developmental stages can be observed in the OCT MIP images of the spinal cord, upper and lower limbs, the brain vesicles, the eye and the heart. The amnion can be seen wrapping the embryo. Somites are also visible lateral to the spinal cord as observed in Fig. 3(a), 3(b). In the corresponding PAT MIP images, the two endogenous absorbers, hemoglobin and melanin, contribute to the signals from the cardiovascular system and the eye, respectively. Besides the vitelline vessels, the dorsal aorta, atrium, ventricle and the pharyngeal arch arteries are all apparent in the background free images. Furthermore, the forming of pectinati muscles in the atrial appendices can be discerned by observing their prints in the blood filling of the atria – from a circularly shaped atrium in Fig. 3(d) to the heavily folded atrium in Fig. 3(f). The pigmented layers of retina of both eyes are visible in the PAT images because of the forward and backward illumination, making this modality a whole-body imaging method. While imaging

the stage HH29 embryo, the effective imaging depth was experimentally determined to be greater than 6.4 mm, which is the thickness of our thickest sample. The OCT imaging depth was 1.2 mm. To validate the OCT/PAT imaging results of chick embryos, virtual resections through the HREM data of these three embryos are shown in Fig. 3(g)-3(i). The organs and vasculature shown by OCT/PAT correspond well with those given by the HREM images.

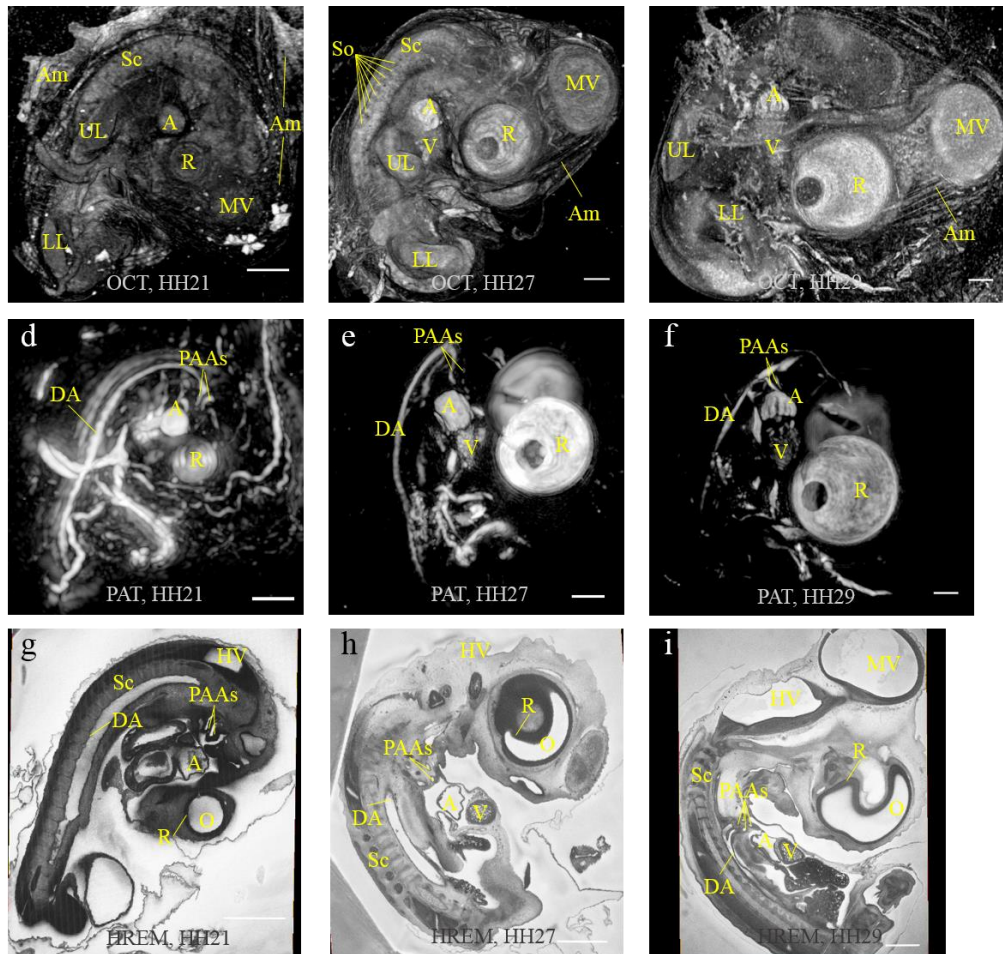


Fig. 3. MIP images of OCT (upper row), PAT (middle row) and HREM slices (lower row) for stage HH21, HH27 and HH29 embryos (from left to right). Sc: spinal cord; A: atrium; V: ventricle; MV: midbrain vesicles; LL: lower limb; UL: upper limb; DA: dorsal aorta; PAAs: pharyngeal arch arteries, HV: hindbrain vesicles; O: optic vesicle; R: retina; So: somites; Am: amnion. Scale bar = 1 mm.

To reveal the 3D co-registered nature of the OCT/PAT imaging, two selected slices at different depths measured from the surface of the sensor for the stage HH21, HH27 and HH29 embryos are shown in Fig. 4 in the left, middle and right columns, respectively. In Fig. 4(a), 4(c) and 4(f) the contour of the heart is provided by OCT, while blood in the chambers of the heart is visualized by PAT. In Fig. 4(d) two pharyngeal arch arteries can be discerned as well as the dorsal aorta. The brain vesicles are seen in OCT, but lack of hemoglobin in these regions renders no PAT signals there. Somites are visible in Fig. 4(e) at a depth of 540 μm . An increased signal from the pigmented retina was detected in later stage embryos, which is confirmed by comparing Fig. 4(a) to Fig. 4(b) and Fig. 4(c). Because the thickness and composition of the retina as well as the pigmentation change during embryo development, this increased signal may reflect an optical property change in this structure.

Due to the small sizes of the blood vessels entering the eyes and the fact that they are not always filled with blood, proper visualization of these vessels is not possible in explanted embryos using PAT. The comparatively huge eyes of chick embryos are encompassed by retina except for the pupil, where the lens develops with a small area on the backside connecting the optic nerve. Since the connection with the optic nerve is tiny, it is not observed in Fig. 4 due to the depth slices selected.

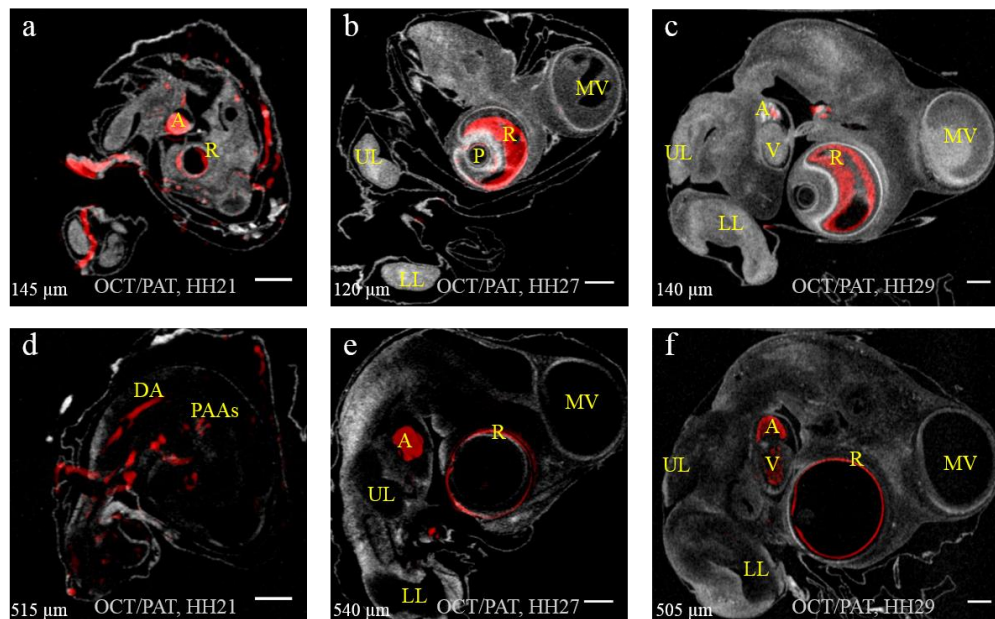


Fig. 4. Two slices of each embryo at various depths (indicated in lower left corner). (a) & (d): stage HH21; (b) & (e): stage HH27; (c) & (f): stage HH29. OCT result displayed in gray scale while PAT result displayed in red. A: atrium; V: ventricle; MV: midbrain vesicles; DA: dorsal aorta; PAAs: pharyngeal arch arteries; R: retina; UL: upper limb; LL: lower limb; P: "pupil" and lens. Scale bar = 1 mm.

Volumetric displays are provided in Fig. 5 for the stage HH21, HH27 and HH29 embryos from left to right, respectively. As in Fig. 4, PAT signals are colored red, and displayed over the gray color mapped OCT volume in Fig. 5(a)-5(c). In Fig. 5(d)-5(f), four major structures are visualized in 3D from the PAT volume data, namely the atrium, the ventricle, the eye and the blood vessels consisting of the dorsal aorta, the pharyngeal arch arteries and the carotid arteries. These four components have been false colored for better visualization. Since the atrial appendices are large and often contain large blood clots, they provided a robust signal in all the three stages. In the lower row, HREM data with a voxel size of $3.4 \mu\text{m} \times 3.4 \mu\text{m} \times 2 \mu\text{m}$ was surface rendered and displayed in 3D to show the fine structures of the intrathoracic arteries. From Fig. 5(d), it is observed that at stage HH21, the primitive atrium and the ventricle are discernable, and the individual pharyngeal arch arteries (right 2nd, 3rd and 4th), right internal carotid artery and the dorsal aorta can be distinguished as long as they are filled with blood. At stage HH27 and HH29, Fig. 5(e), 5(f) show the increase and differentiation of the right atrium and trabeculation of the right ventricle. Pharyngeal arch arteries are partially observable as well as the dorsal aorta, the left internal carotid artery, and at stage HH29 the segments of the two common carotids. At all three stages PAT images show the formation of the pigmentation of the retina very well. All these findings agree with earlier studies [31, 32]. In all the photoacoustic images, blood contrast is from hemoglobin of the erythrocytes. As the embryos develop, the density of blood vessels and their diameters change dramatically, which induces the contrast and differences in the images.

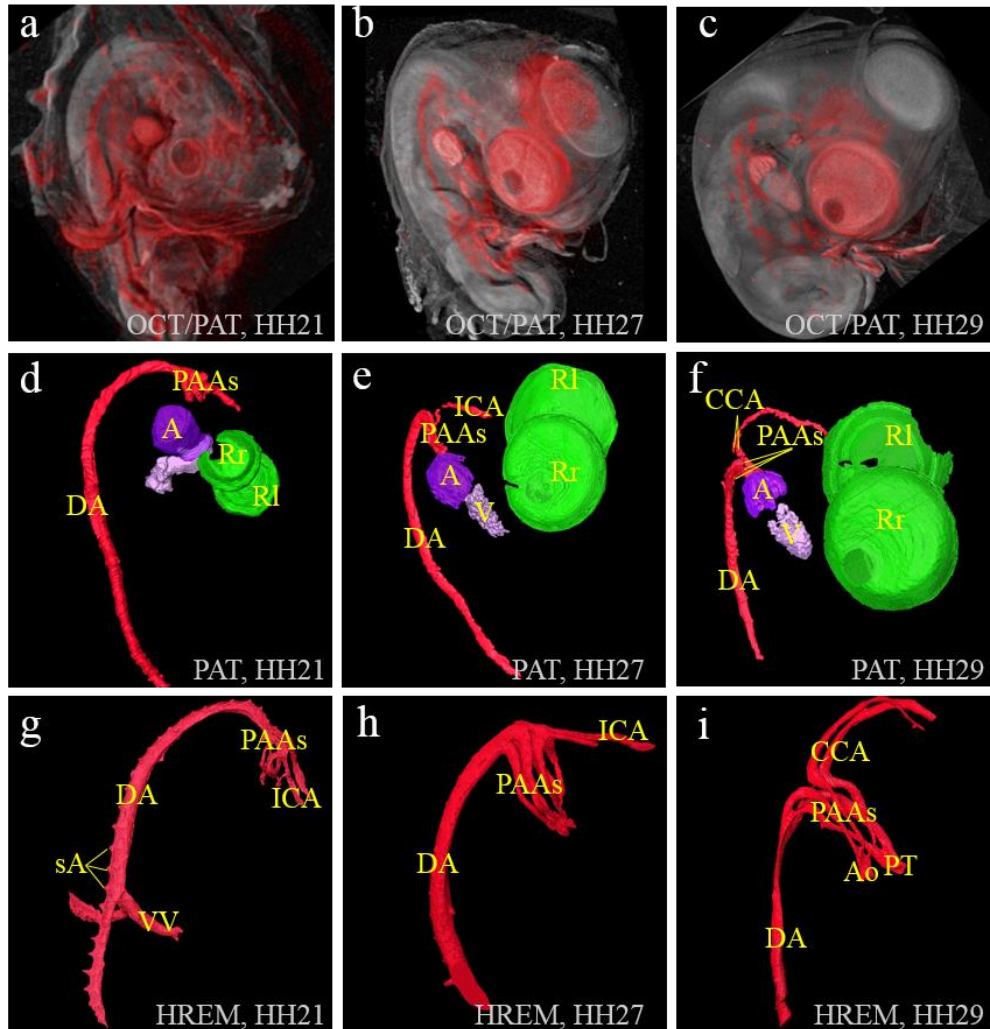


Fig. 5. (a-c): volume display of OCT(gray)/PAT(red) dual modality imaging of the chick embryos of stages HH21, HH27 and HH29, respectively. (d-f): PAT volume displays with eye, atrium, ventricle and blood vessels in false colors for the same embryos as in (a-c). (g-i): HREM volume displays of the blood vessels of the three embryos. PAAAs: pharyngeal arch arteries; ICA: internal carotid artery; sA: segmental arteries, VV: vitelline vessels; Ao: ascending aorta; PT: pulmonary trunk; CCA: common carotid arteries; A: atrium; V: ventricle; R(l&r): (left & right) pigmented layer of retina.

4. Discussion

We have shown that complementary developmental information from the cardiovascular system and additional organs can be acquired with our dual modality OCT/PAT system, utilizing only endogenous contrasts of OCT and PAT. While general morphology of the limbs, eye, spinal cord, body wall, tail and even the amnion is provided with high spatial resolution by OCT, PAT resolved the eye, the blood filled vessel segments throughout the entire embryo and the blood inside the cardiac chambers independent of surrounding structures. Since the embryos lay stable on top of the sensor during imaging, the two modalities' images are inherently co-registered. To our knowledge, this whole-body, dual endogenous contrast, large field of view, co-registered system for visualizing chick embryos

is not achievable by other imaging modalities, making dual modality OCT/PAT imaging a powerful tool for both anatomical and developmental studies using the developing vasculature of chick embryos.

The embryos were explanted from the eggs and placed in paraformaldehyde solution on top of the sensor for imaging, which made it impossible to monitor a single embryo over time. This problem can be addressed by redesigning the sensor holder and inverting the scanning unit. A window into the shell could be cut out to expose the albumen and the yolk, allowing the sensor to be submerged to get closer to the floating embryo. The shell could be heated so that normal development of the embryo can be expected over prolonged time, enabling longitudinal monitoring of chick embryos for drug or developmental studies. We are also investigating the possibility of *ex ovo* but *in vivo* imaging of the chick embryos in shell-less cultures such as the one proposed in [33].

The current duration of each imaging session for a single embryo is an order of magnitude shorter than that of MRI or HREM, but is still too long for functional monitoring of some fast dynamic processes. This is primarily due to the repetition rate of our laser (50Hz). Additionally, it takes approximately 10 minutes to calibrate our sensor prior to imaging each embryo, but we are working to reduce this by a factor of 5 using analog servo boards for our galvanometer scanning mirrors. An alternative approach to reducing overall scanning time would be targeting specific organs, such as the heart, and imaging a smaller volume. This would reduce the active imaging time to ~3 minutes. OCT has already been demonstrated for imaging chick embryo heart in 4D [14], but complementary oxygenation information should be able to be obtained by imaging at multiple wavelengths using PAT [24]. Simultaneous OCT/PAT imaging for late stage chick embryo could still be a challenge though. The fairly large size of the embryo, and the requirement of the planar detector in PAT that detects the photoacoustic pulse originating from the same source at multiple detection points means that more than ten microseconds needs to be waited at each detection point for the acoustic wave to propagate to the sensor. This feature inherently prohibits the PAT system to keep up with our current OCT system which features an A-line rate of 100 kHz. Therefore, for simultaneous OCT/PAT system, not only a photoacoustic excitation laser with fast repetition rate is required, designs other than the planar detector for acoustic waves may also be required.

5. Conclusion and future work

A dual modality optical imaging system combining SS-OCT and whole-body PAT has been demonstrated and applied to chick embryo imaging. Normal embryos from three different development stages were imaged using this dual modality system, whose results not only showed the complementary endogenous scattering and absorption contrast provided by the two sub-modalities, but also the ability of the system to resolve the cardiovascular and morphological changes of the chick embryo at various developmental stages. With redesigned polymer film sensors that feature higher frequency responses and interrogation lasers with higher output power, as well as the reduction of total acquisition time by using analog servo boards for the scanning mirrors, this OCT/PAT system will be invaluable for *in vivo* longitudinal monitoring of angiogenesis, morphogenesis and organogenesis of chick embryos.

Acknowledgment

This project is funded by the Austrian Science Fund (project number S10510-N20) and the European project FAMOS (project number FP7 ICT 317744).